

SBDet: A Symmetry-Breaking Object Detector via Relaxed Rotation-Equivariance

Zhiqiang Wu^{1†} Yingjie Liu^{1†} Hanlin Dong¹
 Xuan Tang² Jian Yang³ Bo Jin¹ Mingsong Chen¹ Xian Wei^{1*}

¹Software Engineering Institute, East China Normal University

²School of Communication and Electronic Engineering, East China Normal University

³School of Geospatial Information, Information Engineering University

Abstract

Introducing Group Equivariant Convolution (GConv) empowers models to explore symmetries hidden in visual data, improving their performance. However, in real-world scenarios, objects or scenes often exhibit perturbations of a symmetric system, specifically a deviation from a symmetric architecture, which can be characterized by a non-trivial action of a symmetry group, known as Symmetry-Breaking. Traditional GConv methods are limited by the strict operation rules in the group space, only ensuring features remain strictly equivariant under limited group transformations, making it difficult to adapt to Symmetry-Breaking or non-rigid transformations. Motivated by this, we introduce a novel Relaxed Rotation GConv (R2GConv) with our defined Relaxed Rotation-Equivariant group \mathbf{R}_4 . Furthermore, we propose a Relaxed Rotation-Equivariant Network (R2Net) as the backbone and further develop the Symmetry-Breaking Object Detector (SBDet) for 2D object detection built upon it. Experiments demonstrate the effectiveness of our proposed R2GConv in natural image classification tasks, and SBDet achieves excellent performance in object detection tasks with improved generalization capabilities and robustness.

1 Introduction

Object detection [57, 28] is a vital computer vision [45] task and is pivotal in various domains, including autonomous driving, geosciences, and ecology. Recent advancements in Deep Neural Networks (DNNs) [39, 42] have made remarkable progress. Nevertheless, objects within natural images often exhibit rotation and scale variations, requiring DNNs to handle geometric transformations more flexibly. For example, in auto-driving scenes, the position and relationship of targets are complex and intricate; objects and the vehicle itself can cause rotation in the scene captured by sensors, seriously affecting target detection performance [18, 50, 29, 54]. More formally, the problem is deemed rotation-equivariant since rotating the input should be anticipated to induce an equivalent rotation in the output. Let $f(\cdot)$ denote the equivariance function for a transformation $g(\cdot)$; it is known that

*Corresponding author: Xian Wei (xwei@tum.de).

† Equal contribution: Zhiqiang Wu and Yingjie Liu.

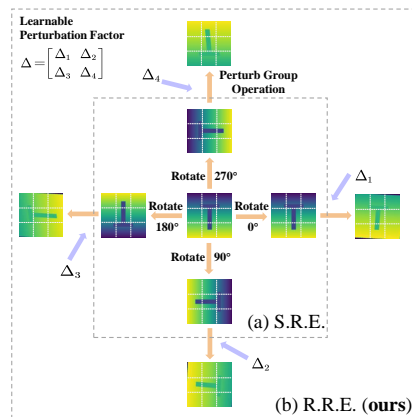


Figure 1: The construction of convolution filters with **Strict** and **Relaxed** Rotation-Equivariance (**S.R.E.** and **R.R.E.**) on the rotation group C_4 .

equivariant functions preserve the symmetry of their input, and we have $f(g(\cdot)) = g(f(\cdot))$. One of the currently effective ways to solve this problem is data augmentation, which aims to improve object detection performance by rotating the dataset, which leads to a considerable cost. Another approach is to build Equivariant Neural Networks (ENNs) [15], which already incorporate symmetries and can focus on the underlying physics. Various ENNs have provided significant improvements for the object detection task.

Although using symmetry as an inductive bias in machine learning has emerged as a powerful tool, with significant conceptual and practical breakthroughs [1], a wide range of learning tasks necessitates Symmetry-Breaking [40]. **However, ENNs cannot effectively model Symmetry-Breaking, as the requirement for equivariance is inherently too restrictive.** Note that the notion of symmetry captures the idea that an object is essentially the same after some transformation is applied to it [51]. For instance, equivariant functions can not break symmetry at the level of *data samples*. Consider a dataset of images with rotational symmetry, where each image depicts a single object that has been rotated. As previously discussed, specific endeavors in ENNs aim to capturing the intrinsic symmetry inherent in images by incorporating the C_2 or C_4 groups. However, these symmetries are restricted to predefined, rigid group operations. When an object experiences symmetry-breaking events, such as rotational deformations beyond the scope of the predefined group or the introduction of minor defects on its surface, a strictly ENN may encounter difficulties in accurately representing these asymmetries. This is because strict adherence to symmetry constraints could prevent it from distinguishing between the object’s perturbed and non-perturbed states, which is crucial for specific tasks. Some pioneer works [33, 41, 47, 27, 22, 53] discussed relaxation of equivariance and claimed that relaxed ENNs can model Symmetry-Breaking in multiple domains. **However, there is still a significant gap between these existing relaxed ENN works and the computer vision field.**

This paper proposes a novel Relaxed Rotation GConv with a **learned** or **controlled** degree of rotation deviation. This relaxation enables the network to recognize the approximate symmetry of the object while capturing the distinct features that arise from perturbations. It facilitates the network’s ability to model Symmetry-Breaking effectively, thereby providing a more nuanced and accurate data representation. To the best of our knowledge, we are the first to address the Symmetry-Breaking problem formally in the object detection scenario. The main contributions of this paper are summarized as follows:

1. We propose a simple yet useful **Relaxed Rotation GConv (R2GConv)** to tackle the trade-off between underlying symmetry-breaking and rotation-equivariance within the image dataset.
2. We propose a redesigned **Symmetry-Breaking Object Detection Network (SBDet)**. To our knowledge, we are the first to explore the symmetry-breaking situation for the object detection task. Experimental experiments demonstrate that our method achieves better convergence and state-of-the-art performance with fewer parameters and better robustness.

2 Related works

2.1 Rotation-Equivariant Neural Networks and Symmetry-Breaking

As a pioneering work, the concept of an equivariant network was proposed in the Group Equivariant Convolution Neural Networks (G-CNN) [5]. Rotation-Equivariant convolution or full connect layer [31, 34, 5, 12] guarantees the rotation-equivariance of extracted features under the group operations by a higher degree of weight sharing. Moreover, the concept of equivariant network is also applied in Graph Neural Networks (GNN) [19, 1], which have demonstrated their prominence in dealing with unarchitected data, such as molecule [14] and point clouds [44].

Although physical laws are governed by numerous symmetries, real-world data, such as complex datasets and graphs, often deviate from strict mathematical symmetry either due to noisy or incomplete data or to inherent Symmetry-Breaking features in the underlying system [41, 47]. Smidt *et al.* [41] show that the gradients of the loss function can be used to learn a Symmetry-Breaking order parameter. Strict constraints on the weights enforce symmetry in equivariant networks. Relaxed equivariant networks constitute another relevant approach, permitting layer weights that enable a departure from strict equivariance. To break symmetry at the level of individual data samples, Wang *et al.* [47] investigate approximately equivariant networks by incorporating relaxed weight sharing in group convolutions and weight-tying in steerable CNNs, respectively, thereby achieving a bias toward

not strictly preserving symmetry. Kaba *et al.* [27] proposes a novel methodology for constructing relaxed equivariant multilayer perceptrons, going beyond the straightforward approach of adding noise to inputs followed by using an equivariant neural network [33]. Huang *et al.* [22] tackled graph symmetry in real-world data by leveraging graph coarsening to establish approximate symmetries and proposing a bias-variance tradeoff formula based on symmetry group selection. Xie *et al.* [53] introduces Symmetry-Breaking parameters sampled as model inputs from a set determined solely by input and output symmetries. They further observe that breaking more symmetry than needed is sometimes beneficial.

2.2 2D Object Detection

With the advent of DNNs and the increasing computational power of GPUs, DNNs have been successfully applied to various computer vision tasks, including object detection [3, 57, 28]. Object detection is a fusion of object location and object classification tasks. It involves locating objects through bounding boxes and identifying their respective categories. Among the different object detection algorithms, the YOLO framework [36, 43, 23] has stood out for its remarkable balance of speed and accuracy, enabling the rapid and reliable identification of objects in images. Since its inception, the YOLO family has evolved through multiple iterations and various other variations, each building upon the previous versions to address limitations and enhance performance. The newest YOLOv8 [26] uses a backbone similar to YOLOv5 [25] and the C2f module to combine high-level features with contextual information to improve detection accuracy. YOLOv8 [26] provided five scaled versions: YOLOv8-n (nano), YOLOv8-s (small), YOLOv8-m (medium), YOLOv8-l (large), and YOLOv8-x (extra-large). In addition to the YOLO framework, the field of object detection and image processing has developed several other notable methods, including RCNN [16], SSD [32], DETR [2], and Transformer-based PVT [48, 49].

Rotation-Equivariance has recently become a strongly desired property in object detection. ReDet [18] incorporates Rotation-Equivariant networks into the detector to extract Rotation-Equivariant features, allowing for accurate orientation prediction and substantially reducing model size. EON [54] introduces a rotation-invariant prior that addresses object detection in 3D scenes, where the bounding box should be equivariant to the object’s pose, regardless of the motion of the scene. TED [52] proposed an efficient transformation-equivariant 3D detector with competitive speed, which comprises a transformation equivariant sparse convolution backbone, transformation-equivariant Bird-Eye-View pooling, and transformation-invariant voxel pooling. DuEqNet [50] improves object detection performance by constructing a dual-layer object detection network for 3D point clouds with rotational invariance and extracting local-global invariance features. FRED [29] further decouples the invariant task (object classification) from the equivariant task (object localization), achieving fully Rotation-Equivariant oriented object detection and enabling more genuine non-axis-aligned learning. These existing equivariant object detection approaches are primarily tailored to 3D point cloud data or specific application contexts. They also overlook scenarios involving necessitating a relaxation of equivariant constraints, i.e., Symmetry-Breaking. This paper further explores a more general 2D object detection in natural images.

3 Method

In the section, we first provide the mathematical definitions of Strict and Relaxed Rotation-Equivariance and briefly review and summarize existing Strict and Relaxed Rotation-Equivariant ENNs, which serve as preliminary knowledge. Then, we describe the main idea of the Relaxed Rotation-Equivariant GConv module. Finally, the Relaxed Rotation-Equivariant object detection network, Symmetry-Breaking Detection Network (SBDet), is introduced and analyzed.

3.1 Preliminary

Definition 1 (Strict Equivariance). A learning function $\Phi_{strict} : \mathcal{X} \rightarrow \mathcal{Y}$ that sends elements from input space \mathcal{X} to output space \mathcal{Y} satisfies Strict Equivariance to a group G if $\forall g, \mathbf{x} \in G \times \mathcal{X}$ there exists $\rho^{\mathcal{X}} : G \rightarrow GL(\mathcal{X})$ and $\rho^{\mathcal{Y}} : G \rightarrow GL(\mathcal{Y})$ actions of G such that

$$\Phi_{strict}(\rho^{\mathcal{X}}(g)\mathbf{x}) = \rho^{\mathcal{Y}}(g)\Phi_{strict}(\mathbf{x}), \quad (1)$$

where $GL(\cdot)$ is a general linear group over the space \cdot .

Definition 2 (Relaxed Equivariance) [47]. A learning function $\Phi_{relaxed} : \mathcal{X} \rightarrow \mathcal{Y}$ that sends elements from input space \mathcal{X} to output space \mathcal{Y} satisfies Relaxed Equivariance to a group G if $\forall g, \mathbf{x} \in G \times \mathcal{X}$ there exists $\rho^{\mathcal{X}} : G \rightarrow GL(\mathcal{X})$ and $\rho^{\mathcal{Y}} : G \rightarrow GL(\mathcal{Y})$ actions of G such that

$$\|\rho^{\mathcal{Y}}(g) \Phi_{relaxed}(\mathbf{x}) - \Phi_{relaxed}(\rho^{\mathcal{X}}(g) \mathbf{x})\| < \epsilon, \quad (2)$$

where ϵ is a controllable variable, with small ϵ exhibiting strong symmetry, while a lot larger ϵ exhibits greater flexibility and generalization ability, as building relaxed convolution filters can be learned from training data. Note that, $\Phi_{relaxed}$ is equivalent to Φ_{strict} when $\epsilon = 0$. Meanwhile, Φ_{strict} satisfies the relaxed equivariance condition.

Strictly Equivariant Neural Networks. Learning equivariant features is an optimization process for a series of Φ_{strict} function sets in the model. Since the composition of equivariant functions is also equivariant, constructing a strict equivariant network is a composition of Φ_{strict} . Simply put, if linear, nonlinear, pooling, aggregation, normalization, and other operators in a network are all equivariant, then their composite operators are also equivariant. However, the challenge of strictly equivariant networks lies in designing trainable linear layers, such as equivariant convolutions. Usually, there are two strategies for designing equivariant convolutions: weight sharing and weight typing, which are G-CNN [5] and G-steerable CNN [6], respectively.

Relaxed Equivariant Neural Networks. The existing equivariant networks assume that the data is completely symmetric. This network approximates a strictly invariant or equivariant function under given group actions. For example, in G-CNN, the shared convolution filter achieves equivariant images at 0, 90, 180, and 270 degrees under the strict constraint of the rotation group \mathbf{C}_4 . However, real-world data is rarely symmetric. This seriously hinders the potential application of equivariant networks. To solve this problem, we can relax the strict constraints on weights under group actions. In [10, 47], relaxing weight constraints can significantly improve the performance and generalization ability of the model.

3.2 The Implementation of Relaxed Rotation-Equivariant GConv (R2GConv)

Relaxing strict group constraints is an effective way to achieve our Relaxed Rotation-Equivariant convolution filters. This paper proposes implementing a learnable parameter Δ to perturb the group operations. Here, our proposed method is based on the fourth-order cyclic rotation group $\mathbf{C}_4 = \{\mathbf{c}^0, \mathbf{c}^1, \mathbf{c}^2, \mathbf{c}^3\}$, where powers of \mathbf{c} indicate performing rotation operation on the input \mathbf{x} by 90 degrees multiple times. The affine transformation matrix $\mathcal{A}_i^{\mathbf{c}}$ on \mathbf{C}_4 can be defined as follows:

$$\mathcal{A}_i^{\mathbf{c}} = \begin{bmatrix} \cos(\pi i/2) & -\sin(\pi i/2) \\ \sin(\pi i/2) & \cos(\pi i/2) \end{bmatrix}, i \in \{0, 1, 2, 3\}. \quad (3)$$

Then, define $\Delta \in \mathbb{R}^{4 \times 2 \times 2}$ denotes our learnable perturbation factor, we have

$$\Delta = \{\Delta_i\} = \left\{ \begin{bmatrix} \Delta_{i1} & \Delta_{i2} \\ \Delta_{i3} & \Delta_{i4} \end{bmatrix} \right\}. \quad (4)$$

Now, we define a Relaxed Rotation-Equivariant group $\mathbf{R}_4 = \{\mathbf{r}^0, \mathbf{r}^1, \mathbf{r}^2, \mathbf{r}^3\}$ based on \mathbf{C}_4 and a function $\mathcal{T} : \mathbf{C}_4 \rightarrow \mathbf{R}_4$. We have a corresponding perturbed affine transformation matrix $\mathcal{A}_i^{\mathbf{r}}$ on \mathbf{R}_4 ,

$$\mathcal{A}_i^{\mathbf{r}} = \mathcal{T}(\mathcal{A}_i^{\mathbf{c}}, \Delta_i) = \begin{bmatrix} \cos(\pi i/2) + \Delta_{i1} & -\sin(\pi i/2) + \Delta_{i2} \\ \sin(\pi i/2) + \Delta_{i3} & \cos(\pi i/2) + \Delta_{i4} \end{bmatrix}, \quad (5)$$

where we use simple addition to add noise to the affine transformation. Note that other operations are also available for \mathcal{T} , such as multiplication but are not limited to. Meanwhile, for all $[a \ b] \in \text{CoordSet}(\mathbf{x})$, we have the transformations $\mathbf{c}^i([a \ b]) = \mathcal{A}_i^{\mathbf{c}} \cdot [a \ b]^{\top}$ and $\mathbf{r}^i([a \ b]) = \mathcal{A}_i^{\mathbf{r}} \cdot [a \ b]^{\top}$ on \mathbf{C}_4 and on \mathbf{R}_4 , respectively. Note that $\text{CoordSet}(\mathbf{x})$ denotes the set of coordinates of \mathbf{x} .

Now we demonstrate the construction of our proposed Relaxed Rotation-Equivariant convolution filters, which is the core of achieving catching symmetric-breaking features.

Given an initial 2D convolution filter \mathcal{K}_{init} , for all $[u \ v] \in \text{CoordSet}(\mathcal{K}_{init})$, and $\mathbf{r}^i \in \mathbf{R}_4$ where $i \in \{0, 1, 2, 3\}$, the transformed coordinates of Relaxed Rotation-Equivariant convolution filters are given as follows:

$$\begin{bmatrix} u' \\ v' \end{bmatrix} = \mathbf{r}^i([u \ v]) = \begin{bmatrix} \cos(\pi i/2) + \Delta_{i1} & -\sin(\pi i/2) + \Delta_{i2} \\ \sin(\pi i/2) + \Delta_{i3} & \cos(\pi i/2) + \Delta_{i4} \end{bmatrix} \begin{bmatrix} u \\ v \end{bmatrix}. \quad (6)$$

We rounded the non-integer coordinates $[u' v']$ to the nearest integer in Equation 6. Further, if $[u' v'] \in \text{CoorSet}(\mathcal{K}_{rel})$, we set $\mathcal{K}_{rel}[u' v'] := \mathcal{K}_{init}[u v]$. All the coordinates of the missing values within \mathcal{K}_{rel} will be performed through *Bilinear* interpolation.

For the detailed construction of \mathcal{K}_{rel} , we provide a pseudocode as shown in Algorithm 1.

Algorithm 1 Build Relaxed Rotation-Equivariant convolution filters based on \mathbf{C}_4 .

Input: Initialized convolution filter: \mathcal{K}_{init} ; The variance of Gaussian distribution: σ
Output: Relaxed Rotation-Equivariant convolution filter: \mathcal{K}_{rel}
Initialize $\mathcal{K}_{rel} \leftarrow \emptyset$
Initialize $\Delta \in \mathbb{R}^{4 \times 2 \times 2}$
 $\Delta \leftarrow \text{Init_Gaussian}(\mathcal{N}(0, \sigma))$ ▷ The initialization of the learnable perturbation factor
 $s \leftarrow \text{Get_Tensor_Shape}(\mathcal{K}_{init})$ ▷ Obtain the tensor shape of \mathcal{K}_{init}
 $c \leftarrow \text{Get_Out_Channels}(\mathcal{K}_{init})$ ▷ Obtain the number of out channels of \mathcal{K}_{init}
for $i = 0$ to 3 **do** ▷ Loop our relaxed group \mathbf{R}_4
 $\mathcal{A} \leftarrow \begin{bmatrix} \cos(\pi i/2) + \Delta[i, 0, 0] & -\sin(\pi i/2) + \Delta[i, 0, 1] & 0 \\ \sin(\pi i/2) + \Delta[i, 1, 0] & \cos(\pi i/2) + \Delta[i, 1, 1] & 0 \end{bmatrix}$ ▷ Affine transformation matrix
 $\mathcal{A}^n \leftarrow \text{Repeat_Tensor}(\mathcal{A}, c)$ ▷ Repeat \mathcal{A} for c times
 $\mathcal{G} \leftarrow \text{Affine_Grid}(\mathcal{A}^n, s)$ ▷ Generate affine grid for \mathcal{A}^n
 $\mathcal{K} \leftarrow \text{Grid_Sample}(\mathcal{K}_{init}, \mathcal{G})$ ▷ Sampling on \mathcal{G} to obtain kernel \mathcal{K}
Update $\mathcal{K}_{rel} \leftarrow \mathcal{K}_{rel} \cup \{\mathcal{K}\}$
end for
return \mathcal{K}_{rel}

So far, we have achieved our Relaxed Rotation-Equivariant convolution filter by relaxing the strict constraints of group operations on \mathbf{C}_4 through our learnable perturbation factor Δ .

Based on it, our following content will introduce Relaxed Rotation-Equivariant GConv (R2GConv), which is divided into two convolutions: Relaxed Rotation-Equivariant Pointwise GConv (R2PGConv) and Relaxed Rotation-Equivariant Depthwise GConv (R2DGConv). The reason for dividing R2GConv into two operators, pointwise and depthwise [4], is to reduce the enormous number of parameters and computational overhead brought by GConv. For convenience, we define the abovementioned algorithm as an operator Φ for generating Relaxed Rotation-Equivariant convolution filters.

Relaxed Rotation-Equivariant Pointwise GConv (R2PGConv). Given that the input image feature map \mathbf{f}_{in} has been projected into the space \mathbf{R}_4 with a size of $c_{in} \times 4 \times h \times w$. Given an initial convolution filter \mathcal{K}_{init}^p with a size of $c_{out} \times c_{in} \times 4 \times 1 \times 1$, we can obtain our Relaxed Rotation-Equivariant pointwise convolution filter $\mathcal{K}_{rel}^p = \Phi(\mathcal{K}_{init}^p)$ with a size of $c_{out} \times 4 \times c_{in} \times 4 \times 1 \times 1$. Then, our R2PGConv can be defined as

$$\mathbf{f}_{out}(c_{out}, 4, h, w) = \sum_c \sum_g \mathcal{K}_{rel}^p(c_{out}, 4, c, g, 1, 1) \star \mathbf{f}_{in}(c, g, h, w), \quad (7)$$

where the size of \mathbf{f}_{out} is $c_{out} \times 4 \times h \times w$, and the operator \star denotes group convolution operation. It is particularly noteworthy that during the convolution operation, \mathcal{K}_{rel}^p will be reshaped to $4c_{out} \times 4c_{in} \times 1 \times 1$, \mathbf{f}_{in} will be reshaped to $4c_{in} \times h \times w$ to meet the input format of the convolution. The output also will be reshaped to $c_{out} \times 4 \times h \times w$. The construction of the convolution filter for R2PGConv is detailed in Figure 2.

Relaxed Rotation-Equivariant Depthwise GConv (R2DGConv). To reduce the huge computational cost of GConv, our R2DGConv adopted the grouped convolution operator. Similar to above, given an initial convolution filter \mathcal{K}_{init}^d with a size of $c_{out} \times 1 \times 1 \times k \times k$, we can obtain our Relaxed Rotation-Equivariant depthwise convolution filter $\mathcal{K}_{rel}^d = \Phi(\mathcal{K}_{init}^d)$ with a size of $c_{out} \times 4 \times 1 \times 1 \times k \times k$. Similarly, our R2DGConv can be defined as

$$\tilde{\mathbf{f}}_{out}(c_{out}, 4, h', w') = \mathcal{K}_{rel}^d(c_{out}, 4, 1, 1, k, k) \star_{gd} \mathbf{f}_{out}(c_{out}, 4, h, w), \quad (8)$$

where the size of $\tilde{\mathbf{f}}_{out}$ is $c_{out} \times 4 \times h' \times w'$, the operator \star_{gd} denotes the grouped convolution, and its number of groups is $4c_{out}$. Also, during the convolution process, \mathcal{K}_{rel}^d will be reshaped to $4c_{out} \times 1 \times k \times k$, \mathbf{f}_{out} will be reshaped to $4c_{out} \times h \times w$.

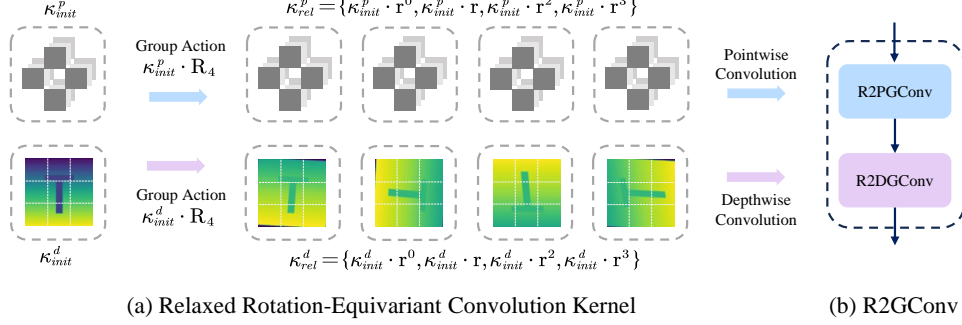


Figure 2: (a): The construction of our Relaxed Rotation-Equivariant convolution filters using the pointwise and depthwise convolution operators. (b): The composition of our R2GConv.

At this point, R2GConv can be defined as follows:

$$\tilde{\mathbf{f}}_{out} = \mathcal{K}_{rel}^d \star_{gd} (\mathcal{K}_{rel}^p \star \mathbf{f}_{in}). \quad (9)$$

Here, the pointwise operation is mainly used for connecting channels, while the depthwise operation reduces the high computational cost. The motivation behind using the pointwise operation first and then the depthwise operation is that the pointwise operation can reduce the number of input channels, thereby reducing the number of the groups of the grouped convolution in the depthwise operation, which ultimately reduces the total parameters of our R2GConv.

3.3 The Relaxed Rotation-Equivariant Network (R2Net)

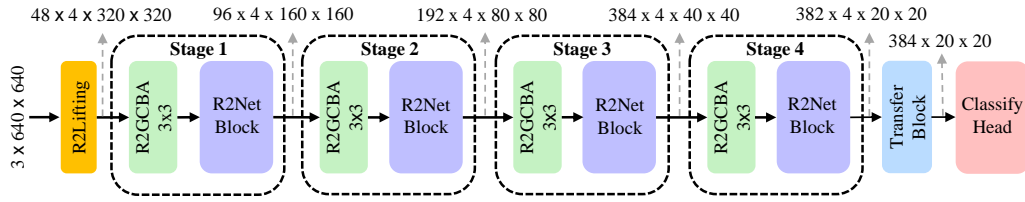


Figure 3: The architecture of our R2Net (Backbone).

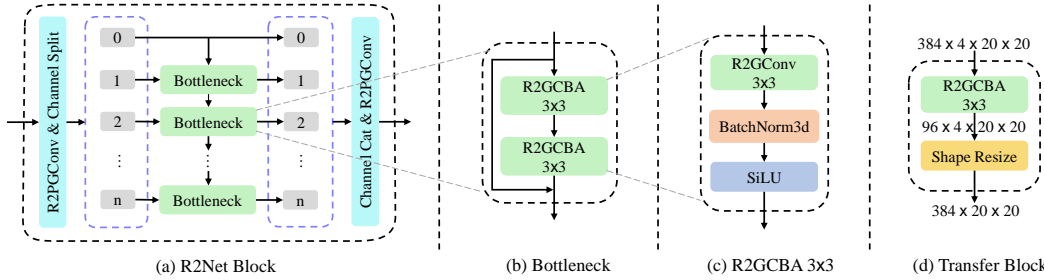


Figure 4: The architecture of our (a) R2Net Block, (b) Bottleneck, (c) R2GCBA 3x3, and (d) Transfer Block. The format of **GCBA3x3** means **G**Conv3x3 \rightarrow **B**atchNorm \rightarrow **A**ctivate.

Based on our R2GConv, we propose a Relaxed Rotation-Equivariant Network (R2Net). Our R2Net (BackBone) consists of four stages: a downsampled R2GCBA3x3 and an R2Net Block. Since the input of a regular CNN is a 2D feature map in the plane \mathbb{Z}^2 space, we typically project the input to \mathbf{R}_4 through our proposed Relaxed Rotation-Equivariant Lifting (R2Lifting) in the first layer. Given a 2D feature map \mathbf{f}_{in} with a size of $c_{in} \times h \times w$ and an initial convolution filter \mathcal{K}_{init}^l with a size of $c_{out} \times c_{in} \times k \times k$, we can obtain our Relaxed Rotation-Equivariant lifting convolution filter $\mathcal{K}_{rel}^l = \Phi(\mathcal{K}_{init}^l)$ with a size of $c_{out} \times 4 \times c_{in} \times k \times k$. Hence, R2Lifting can be defined as

$$\mathbf{f}_{out}(c_{out}, 4, h', w') = \sum_c^{c_{in}} \mathcal{K}_{rel}^l(c_{out}, 4, c, k, k) \star \mathbf{f}_{in}(c, h, w), \quad (10)$$

where the size of \mathbf{f}_{out} is $c_{out} \times 4 \times h' \times w'$, in which h' and w' denote the output height and width, respectively. Again, during the convolution process, \mathcal{K}_{init}^l will be reshaped to $4c_{out} \times c_{in} \times k \times k$, and \mathbf{f}_{in} remains unchanged. Then, input the projected feature map into the 4-layer stage, perform $2\times$ downsampling in sequence, and increase the number of channels by $2\times$. Specifically, the last stage preserves the number of channels unchanged. The obtained output will go through the Transfer Block and then be sent to a universal classification header. The architecture of our R2Net is shown in Figure 3, and the Transfer Block is shown in Figure 4 (d). We provided three models of different sizes in this paper: R2Net-n, R2Net-s, and R2Net-m. More details can be found in Appendix A.1.

Due to the inevitable high computational overhead caused by GConv, we borrow the idea of dividing channels in Res2Net [13] to reduce the number of parameters and FLOPs. The R2Net Block is designed with the residual connection [20] architecture to improve the convergence ability. The detailed module architecture of R2Net Block is shown in Figure 4 (a).

3.4 The Redesigned Symmetry-Breaking Object Detector (SBDet)

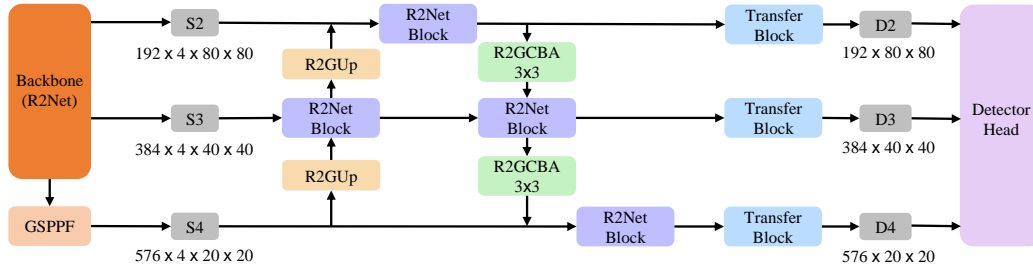


Figure 5: The architecture of SBDet-m.

Based on our proposed R2Net, we propose a Symmetry-Breaking Object Detector (SBDet). SBDet adopts the FPN+PAN neck architecture, taking the stage outputs 2 ~ 4 in R2Net as inputs. Specifically, the input of stage 4 will go through a GSPPF for spatial max pooling under the group C_4 . The obtained inputs are processed through the neck network to obtain multi-scale features, which are then fed into the Transfer Block. Finally, the outputs are fed into a universal detection head of YOLOv8, including three detection heads for detecting small, medium, and large-scale objects. Note that the R2GUp adopts the same architecture as R2GConv, except that the transposed convolution operator is used during the depthwise convolution. The detailed architecture is shown in Figure 5.

4 Experiments

In this section, we conduct extensive experiments to study and demonstrate the performance of the proposed model. In Sec. 4.1, we evaluate our proposed method on the PASCAL VOC and MS COCO 2017 datasets, showing the state-of-the-art performance on the object detection task. We also conduct natural image classification experiments on CIFAR-10/100 dataset, as described in Sec. 4.2. To provide further insight into the effectiveness of our approach, we also present visualization results in Sec. 4.3. The experimental results show that our model has a greater parameter efficiency and accuracy capacity than the existing strict ENNs. We adopt our Relaxed Rotation-Equivariant group R_4 to construct all our models in this section, and a declaration will be made in case of special settings. All the experiments are done on dual GeForce RTX 4090 GPUs.

4.1 Object Detection on the PASCAL VOC and MS COCO Datasets

PASCAL Visual Object Classes (VOC) 2007 comprises 5,000 training images with over 12,000 annotated objects. The PASCAL VOC 2012 expands this with 11,000 training images and 27,000 annotated objects. Both datasets annotate 20 everyday object classes, including person, cat, bicycle, etc. We conduct experiments on the combined PASCAL VOC 07&12. Furthermore, experiments were extended to the Microsoft Common Objects in Context (MS COCO) 2017 dataset, comprised of 164,000 images annotated with 897,000 objects across 80 classes. We aim to validate the capability of our proposed SBDet in standard object detection tasks using mean Average Precision (mAP). Specifically, we leverage \mathbf{mAP}_{50} at an intersection over union (IoU) threshold of 0.5, and $\mathbf{mAP}_{50:90}$ across IoU thresholds ranging from 0.5 to 0.95 as key evaluation metrics.

Table 1: Ablation studies on R.R.E. and S.R.E. in YOLOv8-n and SBDet-n on PASCAL VOC07&12.

Method	R.R.E.	S.R.E.	\mathbf{mAP}_{50}^{val}	$\mathbf{mAP}_{50:95}^{val}$	Params
YOLOv8-n [26]	✗	✗	78.6 _{base}	57.5 _{base}	3.2M
	✗	✓	82.7 _{+4.1}	62.8 _{+5.3}	3.3M
	✓	✗	83.6 _{+5.0}	64.2 _{+6.7}	3.3M
SBDet-n (ours)	✗	✗	77.9 _{base}	57.0 _{base}	2.4M
	✗	✓	83.0 _{+5.1}	63.0 _{+6.0}	2.6M
	✓	✗	84.1 _{+6.2}	64.6 _{+7.6}	2.6M

Table 2: Performance of SBDet-n on PASCAL VOC 07&12 for different variance σ .

σ	\mathbf{mAP}_{50}^{val}	$\mathbf{mAP}_{50:95}^{val}$
0.1	84.1	64.6
0.2	83.5	64.3
0.4	83.6	64.4
0.6	82.4	62.6
0.8	80.7	59.7

We conduct ablation analyses on Relaxed Rotation Equivariance (R.R.E.) and Strict Rotation Equivariance (S.R.E.) in YOLOv8-n and our proposed SBDet-n. As shown in Table 1, when both R.R.E. and S.R.E. are disabled, the baseline \mathbf{mAP}_{50} scores of YOLOv8-n and SBDet-n are 78.6 and 77.9 respectively. When enabling R.R.E. (or S.R.E.), the \mathbf{mAP}_{50} scores increase by 5% and 6.2% (or 4.1% and 5.1%) respectively, indicating that R.R.E. and S.R.E. improve the accuracy of object detection. However, the \mathbf{mAP}_{50} improvement of R.R.E. is greater than that of S.R.E. both in SBDet-n and YOLOv8-n, indicating the effectiveness of our R.R.E. The same situation also occurs on the $\mathbf{mAP}_{50:95}$ improvement. To investigate further the effect of different initial parameters σ on the performance of SBDet-n, we perform experiments with various values of σ ranging from 0.1 to 0.8. As shown in Table 2, when σ is set to 0.1, 0.2, or 0.4, mAP fluctuates little, but when σ is set to 0.6 or 0.8, mAP decreases significantly. Refer to Appendix A.2 for model convergence details across various σ . Note that σ is set to 0.1 in the following.

Table 3 presents the PASCAL VOC 07&12 test results. Notably, our SBDet-m (22.6M) stands out with its remarkable performance, boasting the highest 87.3% \mathbf{mAP}_{50} , and 70.6% $\mathbf{mAP}_{50:95}$ among the listed models. Notably our SBDet-m achieves an increase in \mathbf{mAP}_{50} (and $\mathbf{mAP}_{50:95}$) by 0.4% (and 1.1%) compared to YOLOv8-x, also having only 33.1% parameters of YOLOv8-x (68.2M). In addition, our SBDet-n has the least parameters but with good results.

We also conduct experiments on a larger dataset, MS COCO 2017, as shown in Table 4. Our SBDet-n (2.8M) achieved a surprising improvement in $\mathbf{mAP}_{50:95}$ (and \mathbf{mAP}_{50}) by 6.2% (and 6.4%) compared to YOLOv6-n, despite having only 59.6% parameters of YOLOv6-n (4.7M). Furthermore, our SBDet-s achieved slightly lower (or equal) $\mathbf{mAP}_{50:95}$ and \mathbf{mAP}_{50} compared to YOLOv8-m (or YOLOv6-m), but only with about 33.3% of their parameters. Similarly, our SBDet-m achieved an approximate \mathbf{mAP}_{50} and $\mathbf{mAP}_{50:95}$ compared to YOLOv8-l, but with about a half parameters of YOLOv8-l. It can be seen that our SBDet has fewer parameters and higher accuracy.

SBDet excels in the trade-off between efficiency and accuracy. Further details on convergence analyses and loss curve experiments are provided in Appendix A.3.

Table 3: PASCAL VOC 07&12 test results.

Method	\mathbf{mAP}_{50}^{test}	$\mathbf{mAP}_{50:95}^{test}$	Params	FLOPs
Faster RCNN [17]	73.2	-	41.1M	-
LMSN300 [56]	75.8	-	24.08M	-
SSD300 [32]	77.5	-	26.3M	31.4G
SSD512 [32]	78.5	-	26.3M	31.4G
FSSD [35]	78.8	-	34.1M	38.1G
R-FCN [7]	80.5	-	80.5M	-
YOLOv2 [37]	76.8	-	50.7M	14.7G
YOLOv3 [38]	79.3	-	33.1M	62.0G
SlimYOLOv4 [9]	70.8	-	8.1M	3.2G
L-YOLOv4 [8]	74.9	-	10.4M	4.9G
η -RepYOLO [11]	84.8	-	10.8M	26.5G
η -RepYOLO [11]	85.7	-	8.8M	23.2G
YOLOv8-n [26]	78.6	57.5	3.0M	8.1G
YOLOv8-s [26]	81.6	61.6	11.1M	28.5G
YOLOv8-m [26]	83.7	65.3	25.9M	78.7G
YOLOv8-l [26]	86.4	69.0	43.6M	164.9G
YOLOv8-x [26]	86.9	69.5	68.1M	257.5G
SBDet-n (ours)	84.1	64.7	2.6M	3.3G
SBDet-s (ours)	86.0	68.4	9.6M	8.9G
SBDet-m (ours)	87.3	70.6	22.6M	17.2G

Table 4: MS COCO 2017 validation results.

Method	\mathbf{mAP}_{50}^{val}	$\mathbf{mAP}_{50:95}^{val}$	Params	FLOPs
YOLOv5-n [25]	45.7	28.0	1.9M	4.5M
YOLOv5-s [25]	56.8	37.4	7.2M	16.5M
YOLOv5-m [25]	64.1	45.4	21.2M	49.0M
YOLOv5-l [25]	67.3	49.0	46.5M	109.1M
YOLOv5-x [25]	68.9	50.7	86.7M	205.7M
YOLOv6-n [30]	53.1	37.5	4.7M	11.4G
YOLOv6-s [30]	61.8	45.0	18.5M	45.3G
YOLOv6-m [30]	66.9	50.0	34.9M	85.8G
YOLOv6-l [30]	70.3	52.8	59.6M	150.7G
YOLOv7-tiny [46]	55.2	37.4	6.2M	13.7G
YOLOv7 [46]	69.7	51.2	36.9M	104.7G
YOLOv8-n [26]	52.6	37.3	3.2M	8.7G
YOLOv8-s [26]	61.8	44.9	11.2M	28.6G
YOLOv8-m [26]	67.2	50.2	25.9M	78.9G
YOLOv8-l [26]	69.8	52.9	43.7M	165.2G
YOLOv8-x [26]	71.0	53.9	68.2M	257.8G
SBDet-n (ours)	59.5	43.7	2.8M	4.0G
SBDet-s (ours)	66.5	50.0	9.6M	9.0G
SBDet-m (ours)	69.6	52.7	22.6M	17.3G

4.2 Image Classification on the CIFAR-10/100 and Rotated MNIST Datasets

In this section, we evaluate the performance of our proposed R2Net on image classification tasks using the CIFAR-10/100 and Rotated MNIST datasets, where we randomly rotate all images in the MNIST training set by 0, 90, 180, and 270 degrees, leaving the test set unaffected. As seen from Table 5, our R2Net-n achieves competitive results compared to other models while having much smaller parameters (0.8M). Our R2Net-m achieved a top-1 test error rate of only 3.5% on CIFAR-10 and 17.3% on CIFAR-100, slightly lower than ResNeXt-29, but with only 6M parameters, which is 10% parameters of ResNeXt-29. Furthermore, our R2Net-x outperforms all other models with a top-1 test error rate of only 3.33% on CIFAR-10 and 16.1% on CIFAR-100. Additionally, we also evaluate the performance of our R2Net on the Rotated MNIST dataset. As shown in Table 6, Our R2Net-n achieves a top-1 test error rate of 27.75%, outperforming YOLOv8-n-cls in recognizing rotated images. Overall, these results demonstrate the superior performance of our proposed R2Net in image classification tasks on both standard and rotated datasets.

Table 5: Top-1 test error (%) on CIFAR-10/100 dataset.

Method	CIFAR-10	CIFAR-100	Params
WideResNet [55]	4.17	20.50	36.5M
ResNeXt-29 [20]	3.58	17.31	68.1M
Res2NeXt-29 [13]	-	16.79	36.7M
DenseNet-BC [21]	3.46	17.18	25.6M
R2Net-n (ours)	7.30	19.30	0.8M
R2Net-m (ours)	3.50	17.30	6.0M
R2Net-x (ours)	3.33	16.10	20.4M

Table 6: Top-1 test error (%) on MNIST (M.) and Rotated MNIST (R.M.) dataset.

Method	Dataset	Error	Params
YOLOv8-n-cls [26]	M.	0.58	1.5M
	R.M.	44.88	
R2Net-n (ours)	M.	0.54	0.8M
	R.M.	27.75	

4.3 Relaxed, Strict Rotation-Equivariance and Non-Rotation-Equivariance Visualization

The visualization of our R.R.E., S.R.E., and Non-Rotation-Equivariance (N.R.E.) is shown in Figure 6. We rotate the original image (a) to obtain rotated images (b) and input them into our SBDet (R.R.E.), SBDet (S.R.E.), and YOLOv8 (N.R.E.) to obtain the feature maps (c), (d), and (e), respectively. Observing the white circles in (c), we notice slight differences. Nevertheless, the overall feature maps are Rotation-Equivariant, showcasing our R.R.E. Observing the red circles in (d), we find that the feature maps are strictly equivariant, presenting S.R.E. Lastly, observing (e), we find almost N.R.E. A more detailed visualization of R.R.E. in our SBDet-n can be found in Appendix A.6.

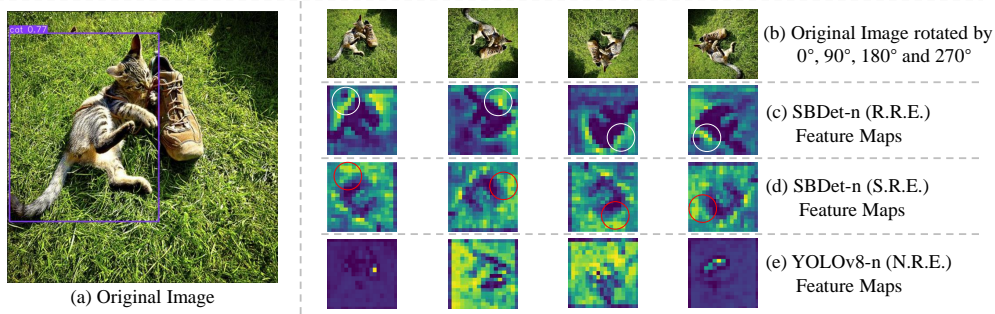


Figure 6: Visualization of feature maps in SBDet-n (R.R.E. and S.R.E.) and YOLOv8-n (N.R.E.).

5 Conclusion

In this work, we propose Relaxed Rotation-Equivariant Group Convolution (R2GConv), a novel approach that tackles symmetry-breaking situations in rotation-equivariance to better align with real-world scenarios. R2GConv introduces learnable parameters to transform a strict rotation-equivariant group C_4 into a relaxed rotation-equivariant group R_4 by perturbing group operations. Furthermore, we propose an efficient Relaxed Rotation-Equivariant Network (R2Net) as the backbone and a redesigned 2D object detector called Symmetry-Breaking Object Detector (SBDet). Through experiments on the object detection and classification tasks, we demonstrate that our proposed SBDet and R2Net achieve state-of-the-art performance compared to models without symmetry bias or with strict equivariant constraints. However, a limitation is the relatively slower training speed, so integrating CUDA-accelerated operations is one of the future directions. Additionally, R2GConv or R2Net can be applied to more complex visual tasks and scenes, leveraging the advantages of Relaxed Rotation-Equivariance.

References

- [1] Michael M Bronstein, Joan Bruna, Taco Cohen, and Petar Veličković. Geometric deep learning: Grids, groups, graphs, geodesics, and gauges. *arXiv preprint arXiv:2104.13478*, 2021.
- [2] Nicolas Carion, Francisco Massa, Gabriel Synnaeve, Nicolas Usunier, Alexander Kirillov, and Sergey Zagoruyko. End-to-end object detection with transformers. In *European conference on computer vision*, pages 213–229. Springer, 2020.
- [3] Wei Chen, Yan Li, Zijian Tian, and Fan Zhang. 2d and 3d object detection algorithms from images: A survey. *Array*, page 100305, 2023.
- [4] François Chollet. Xception: Deep learning with depthwise separable convolutions. In *Proceedings of the IEEE conference on computer vision and pattern recognition*, pages 1251–1258, 2017.
- [5] Taco Cohen and Max Welling. Group equivariant convolutional networks. In *International conference on machine learning*, pages 2990–2999. PMLR, 2016.
- [6] Taco S. Cohen and Max Welling. Steerable cnns. *CoRR*, abs/1612.08498, 2016.
- [7] Jifeng Dai, Yi Li, Kaiming He, and Jian Sun. R-fcn: Object detection via region-based fully convolutional networks. *Advances in neural information processing systems*, 29, 2016.
- [8] Peng Ding, Huaming Qian, Jiabing Bao, Yipeng Zhou, and Shuya Yan. L-yolov4: lightweight yolov4 based on modified rfb-s and depthwise separable convolution for multi-target detection in complex scenes. *Journal of Real-Time Image Processing*, 20(4):71, 2023.
- [9] Peng Ding, Huaming Qian, and Shuai Chu. Slimyolov4: lightweight object detector based on yolov4. *Journal of Real-Time Image Processing*, 19(3):487–498, 2022.
- [10] Gamaleldin F. Elsayed, Prajit Ramachandran, Jonathon Shlens, and Simon Kornblith. Revisiting spatial invariance with low-rank local connectivity. *CoRR*, abs/2002.02959, 2020.
- [11] Shuai Feng, Huaming Qian, Huilin Wang, and Wenna Wang. η -repyolo: real-time object detection method based on η -repconv and yolov8. *Journal of Real-Time Image Processing*, 21(3):1–14, 2024.
- [12] Marc Finzi, Samuel Stanton, Pavel Izmailov, and Andrew Gordon Wilson. Generalizing convolutional neural networks for equivariance to lie groups on arbitrary continuous data. In *International Conference on Machine Learning*, pages 3165–3176. PMLR, 2020.
- [13] Shang-Hua Gao, Ming-Ming Cheng, Kai Zhao, Xin-Yu Zhang, Ming-Hsuan Yang, and Philip Torr. Res2net: A new multi-scale backbone architecture. *IEEE Transactions on Pattern Analysis and Machine Intelligence*, 43(2):652–662, 2019.
- [14] Johannes Gasteiger, Janek Groß, and Stephan Günnemann. Directional message passing for molecular graphs. *arXiv preprint arXiv:2003.03123*, 2020.
- [15] Jan E Gerken, Jimmy Aronsson, Oscar Carlsson, Hampus Linander, Fredrik Ohlsson, Christoffer Petersson, and Daniel Persson. Geometric deep learning and equivariant neural networks. *Artificial Intelligence Review*, 56(12):14605–14662, 2023.
- [16] Ross Girshick, Jeff Donahue, Trevor Darrell, and Jitendra Malik. Rich feature hierarchies for accurate object detection and semantic segmentation. In *Proceedings of the IEEE conference on computer vision and pattern recognition*, pages 580–587, 2014.
- [17] Ross B. Girshick. Fast R-CNN. *CoRR*, abs/1504.08083, 2015.
- [18] Jiaming Han, Jian Ding, Nan Xue, and Gui-Song Xia. Redet: A rotation-equivariant detector for aerial object detection. In *Proceedings of the IEEE/CVF conference on computer vision and pattern recognition*, pages 2786–2795, 2021.
- [19] Jiaqi Han, Yu Rong, Tingyang Xu, and Wenbing Huang. Geometrically equivariant graph neural networks: A survey. *arXiv preprint arXiv:2202.07230*, 2022.
- [20] Kaiming He, Xiangyu Zhang, Shaoqing Ren, and Jian Sun. Deep residual learning for image recognition. In *Proceedings of the IEEE conference on computer vision and pattern recognition*, pages 770–778, 2016.
- [21] Gao Huang, Zhuang Liu, Laurens Van Der Maaten, and Kilian Q Weinberger. Densely connected convolutional networks. In *Proceedings of the IEEE conference on computer vision and pattern recognition*, pages 4700–4708, 2017.

- [22] Ningyuan Huang, Ron Levie, and Soledad Villar. Approximately equivariant graph networks. *Advances in Neural Information Processing Systems*, 36, 2024.
- [23] Muhammad Hussain. Yolo-v1 to yolo-v8, the rise of yolo and its complementary nature toward digital manufacturing and industrial defect detection. *Machines*, 11(7):677, 2023.
- [24] Peng-Tao Jiang, Chang-Bin Zhang, Qibin Hou, Ming-Ming Cheng, and Yunchao Wei. Layercam: Exploring hierarchical class activation maps for localization. *IEEE Transactions on Image Processing*, 30:5875–5888, 2021.
- [25] Glenn Jocher. YOLOv5 by Ultralytics, May 2020.
- [26] Glenn Jocher, Ayush Chaurasia, and Jing Qiu. Ultralytics YOLO, January 2023.
- [27] Sékou-Oumar Kaba and Siamak Ravanbakhsh. Symmetry breaking and equivariant neural networks. *arXiv preprint arXiv:2312.09016*, 2023.
- [28] Ravpreet Kaur and Sarbjeet Singh. A comprehensive review of object detection with deep learning. *Digital Signal Processing*, 132:103812, 2023.
- [29] Chanho Lee, Jinsu Son, Hyounguk Shon, Yunho Jeon, and Junmo Kim. Fred: Towards a full rotation-equivariance in aerial image object detection. In *Proceedings of the AAAI Conference on Artificial Intelligence*, volume 38, pages 2883–2891, 2024.
- [30] Chuyi Li, Lulu Li, Hongliang Jiang, Kaiheng Weng, Yifei Geng, Liang Li, Zaidan Ke, Qingyuan Li, Meng Cheng, Weiqliang Nie, et al. Yolov6: A single-stage object detection framework for industrial applications. *arXiv preprint arXiv:2209.02976*, 2022.
- [31] Junying Li, Zichen Yang, Haifeng Liu, and Deng Cai. Deep rotation equivariant network. *Neurocomputing*, 290:26–33, 2018.
- [32] Wei Liu, Dragomir Anguelov, Dumitru Erhan, Christian Szegedy, Scott Reed, Cheng-Yang Fu, and Alexander C Berg. Ssd: Single shot multibox detector. In *Computer Vision—ECCV 2016: 14th European Conference, Amsterdam, The Netherlands, October 11–14, 2016, Proceedings, Part I 14*, pages 21–37. Springer, 2016.
- [33] Francesco Locatello, Dirk Weissenborn, Thomas Unterthiner, Aravindh Mahendran, Georg Heigold, Jakob Uszkoreit, Alexey Dosovitskiy, and Thomas Kipf. Object-centric learning with slot attention. *Advances in Neural Information Processing Systems*, 33:11525–11538, 2020.
- [34] Diego Marcos, Michele Volpi, Nikos Komodakis, and Devis Tuia. Rotation equivariant vector field networks. In *Proceedings of the IEEE International Conference on Computer Vision*, pages 5048–5057, 2017.
- [35] Huaming Qian, Huilin Wang, Shuai Feng, and Shuya Yan. Fessd: Ssd target detection based on feature fusion and feature enhancement. *Journal of Real-Time Image Processing*, 20(1):2, 2023.
- [36] Joseph Redmon, Santosh Divvala, Ross Girshick, and Ali Farhadi. You only look once: Unified, real-time object detection. In *Proceedings of the IEEE conference on computer vision and pattern recognition*, pages 779–788, 2016.
- [37] Joseph Redmon and Ali Farhadi. YOLO9000: better, faster, stronger. *CoRR*, abs/1612.08242, 2016.
- [38] Joseph Redmon and Ali Farhadi. Yolov3: An incremental improvement. *CoRR*, abs/1804.02767, 2018.
- [39] Wojciech Samek, Grégoire Montavon, Sebastian Lapuschkin, Christopher J Anders, and Klaus-Robert Müller. Explaining deep neural networks and beyond: A review of methods and applications. *Proceedings of the IEEE*, 109(3):247–278, 2021.
- [40] Tess E. Smidt, Mario Geiger, and Benjamin Kurt Miller. Finding symmetry breaking order parameters with euclidean neural networks. *Phys. Rev. Research*, 3:L012002, Jan 2021.
- [41] Tess E Smidt, Mario Geiger, and Benjamin Kurt Miller. Finding symmetry breaking order parameters with euclidean neural networks. *Physical Review Research*, 3(1):L012002, 2021.
- [42] Vivienne Sze, Yu-Hsin Chen, Tien-Ju Yang, and Joel S Emer. Efficient processing of deep neural networks: A tutorial and survey. *Proceedings of the IEEE*, 105(12):2295–2329, 2017.

- [43] Juan Terven, Diana-Margarita Córdova-Esparza, and Julio-Alejandro Romero-González. A comprehensive review of yolo architectures in computer vision: From yolov1 to yolov8 and yolo-nas. *Machine Learning and Knowledge Extraction*, 5(4):1680–1716, 2023.
- [44] Nathaniel Thomas, Tess Smidt, Steven Kearnes, Lusann Yang, Li Li, Kai Kohlhoff, and Patrick Riley. Tensor field networks: Rotation-and translation-equivariant neural networks for 3d point clouds. *arXiv preprint arXiv:1802.08219*, 2018.
- [45] Athanasios Voulodimos, Nikolaos Doulamis, Anastasios Doulamis, and Eftychios Protopapadakis. Deep learning for computer vision: A brief review. *Computational intelligence and neuroscience*, 2018, 2018.
- [46] Chien-Yao Wang, Alexey Bochkovskiy, and Hong-Yuan Mark Liao. Yolov7: Trainable bag-of-freebies sets new state-of-the-art for real-time object detectors. In *Proceedings of the IEEE/CVF conference on computer vision and pattern recognition*, pages 7464–7475, 2023.
- [47] Rui Wang, Robin Walters, and Rose Yu. Approximately equivariant networks for imperfectly symmetric dynamics. In *International Conference on Machine Learning*, pages 23078–23091. PMLR, 2022.
- [48] Wenhai Wang, Enze Xie, Xiang Li, Deng-Ping Fan, Kaitao Song, Ding Liang, Tong Lu, Ping Luo, and Ling Shao. Pyramid vision transformer: A versatile backbone for dense prediction without convolutions. In *Proceedings of the IEEE/CVF international conference on computer vision*, pages 568–578, 2021.
- [49] Wenhai Wang, Enze Xie, Xiang Li, Deng-Ping Fan, Kaitao Song, Ding Liang, Tong Lu, Ping Luo, and Ling Shao. Pvt v2: Improved baselines with pyramid vision transformer. *Computational Visual Media*, 8(3):415–424, 2022.
- [50] Xihao Wang, Jiaming Lei, Hai Lan, Arafat Al-Jawari, and Xian Wei. Dueqnet: dual-equivariance network in outdoor 3d object detection for autonomous driving. In *2023 IEEE International Conference on Robotics and Automation (ICRA)*, pages 6951–6957. IEEE, 2023.
- [51] Hermann Weyl. Symmetry. In *Symmetry*. Princeton University Press, 1952.
- [52] Hai Wu, Chenglu Wen, Wei Li, Xin Li, Ruigang Yang, and Cheng Wang. Transformation-equivariant 3d object detection for autonomous driving. In *Proceedings of the AAAI Conference on Artificial Intelligence*, volume 37, pages 2795–2802, 2023.
- [53] YuQing Xie and Tess Smidt. Equivariant symmetry breaking sets. *arXiv preprint arXiv:2402.02681*, 2024.
- [54] Hong-Xing Yu, Jiajun Wu, and Li Yi. Rotationally equivariant 3d object detection. In *Proceedings of the IEEE/CVF Conference on Computer Vision and Pattern Recognition*, pages 1456–1464, 2022.
- [55] Sergey Zagoruyko and Nikos Komodakis. Wide residual networks. *arXiv preprint arXiv:1605.07146*, 2016.
- [56] Yiye Zou, Xiaomin Yang, Marcelo Keese Albertini, and Farhan Hussain. Lmsn: a lightweight multi-scale network for single image super-resolution. *Multimedia Systems*, 27:845–856, 2021.
- [57] Zhengxia Zou, Keyan Chen, Zhenwei Shi, Yuhong Guo, and Jieping Ye. Object detection in 20 years: A survey. *Proceedings of the IEEE*, 111(3):257–276, 2023.

A Appendix

A.1 Model architecture of SBDet

In this section, we provide a detailed construction of our SBDets of different sizes, as shown in Table 7.

Table 7: The model architecture of our SBDet-n, SBDet-s, and SBDet-m. Among them, the **NO.** column shows the number of layers; The **From** column indicates where the input of this layer module comes from. For example, -1 represents the upper layer, -1, 6 represents the upper layer, and layer 6. Note that in the **Output Size** column, $\times 4$ denotes the group dimension, not the number of channels. **O.C.** denotes Output channels in the table below.

No.	From	Module	Output Size	SBDet-n		SBDet-s		SBDet-m	
				O.C.	Params	O.C.	Params	O.C.	Params
0	-1	R2Lifting	$4 \times 320 \times 320$	16	480	32	944	48	1408
1	-1	R2GCBA3x3	$4 \times 160 \times 160$	32	2416	64	8912	96	19504
2	-1	R2Net Block	$4 \times 160 \times 160$	32	9640	64	37680	96	131152
3	-1	R2GCBA3x3	$4 \times 80 \times 80$	64	8912	128	34192	192	75856
4	-1	R2Net Block	$4 \times 80 \times 80$	64	58784	128	232192	192	409664
5	-1	R2GCBA3x3	$4 \times 40 \times 40$	128	34192	256	133904	384	299152
6	-1	R2Net Block	$4 \times 40 \times 40$	128	232192	256	923072	384	1630208
7	-1	R2GCBA3x3	$4 \times 20 \times 20$	128	66960	256	264976	384	594064
8	-1	R2Net Block	$4 \times 20 \times 20$	128	149056	256	592992	384	2072704
9	-1	GSPPF	$4 \times 20 \times 20$	128	65792	256	262656	384	590592
10	-1	R2GUp	$4 \times 40 \times 40$	64	33040	128	131600	192	295696
11	-1, 6	GConcat	$4 \times 40 \times 40$	192	0	384	0	576	0
12	-1	R2Net Block	$4 \times 40 \times 40$	128	181824	256	724064	384	2515072
13	-1	R2GUp	$4 \times 80 \times 80$	64	33040	128	131600	192	295696
14	-1, 4	GConcat	$4 \times 80 \times 80$	128	0	256	0	384	0
15	-1	R2Net Block	$4 \times 80 \times 80$	64	54064	128	214592	192	741472
16	-1	R2GCBA3x3	$4 \times 40 \times 40$	64	17104	128	66960	192	149584
17	-1, 12	GConcat	$4 \times 40 \times 40$	192	0	384	0	576	0
18	-1	R2Net Block	$4 \times 40 \times 40$	128	181824	256	724064	384	2515072
19	-1	R2GCBA3x3	$4 \times 20 \times 20$	128	66960	256	264976	384	594064
20	-1, 9	GConcat	$4 \times 20 \times 20$	256	0	512	0	768	0
21	-1	R2Net Block	$4 \times 20 \times 20$	256	592992	512	2365600	576	5320864
22	15	Transfer Block	80×80	64	4288	128	16752	192	37408
23	18	Transfer Block	40×40	128	16752	256	66256	384	148528
24	21	Transfer Block	20×20	256	66256	512	263568	576	333376
25	22, 23, 24	Detector Head	-	-	897664	-	2147008	-	3822016
Total Params				2.8M		9.6M		22.6M	
FLOPs				4.0G		9.0G		17.3G	

A.2 Convergence Analysis on SBDet models with different σ

In this section, we further conduct a convergence analysis on the learnable perturbation factor by examining the impact of varying the variance σ of its initial Gaussian distribution in our SBDet-n model on the PASCAL VOC dataset. As illustrated in Figure 7, it is clear that when σ values are set to 0.1, 0.2, and 0.4, the convergence behavior of the model remains consistent across these values, ultimately converging to similar accuracy in **mAP**₅₀ (and **mAP**_{50:95}). The highest accuracy is observed with the variance $\sigma = 0.1$. However, for σ values set to 0.6 and 0.8, there is a lot of decrease in model accuracy, particularly with $\sigma = 0.8$ exhibiting the lowest accuracy. We speculate that for larger initial σ , there is too much perturbation to the group operation, which leads to a significant degree of Symmetry-Breaking in the model, making it difficult for the model to learn the appropriate degree of Symmetry-Breaking from the training dataset, resulting in lower accuracy.

A.3 Supplemental Convergence Analysis on SBDet models

In this section, we analyze the accuracy and loss curves of the SBDet and YOLOv8 models during the training process on the PASCAL VOC dataset, as detailed in Figure 8. In part (a), it is evident that our SBDet model

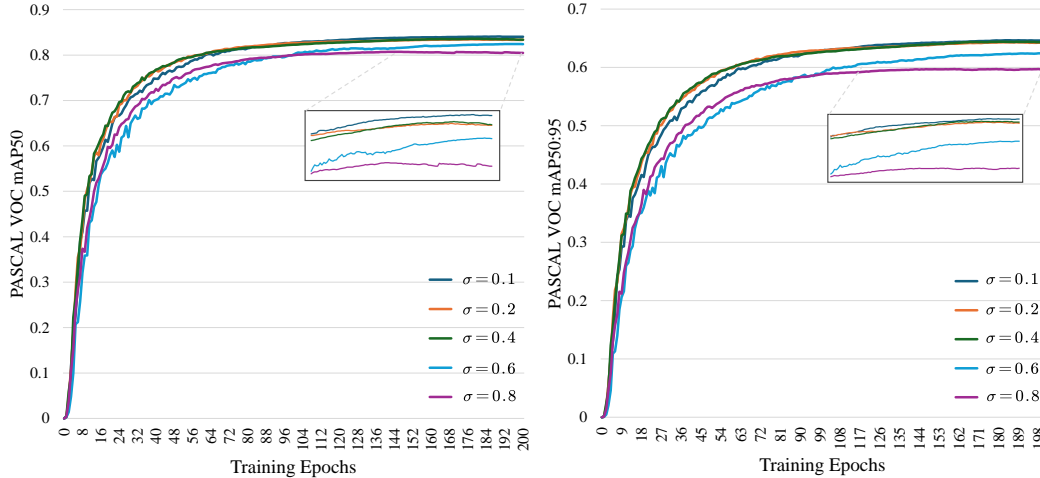


Figure 7: Comparison of SBDet-n with different σ . All models were trained for 200 epochs on dual 4090 GPUs.

exhibits not only a more stable training process but also surpasses the accuracy of outstanding YOLOv8 models. Moreover, our model achieves faster convergence, significantly reducing the total number of training epochs needed to reach the target accuracy, which it attains within approximately 90 to 100 epochs. The fast convergence could be related to the fact that our R2GCCConv can extract rich and relaxed equivariant features, hence enabling earlier learning of these potential features. Regarding the loss function, both YOLOv8 and SBDet exhibit a steady decline across all three loss components, as illustrated in parts (b), (c), and (d) of the figure.

A.4 Supplemental Experiments on PASCAL VOC 07&12 dataset

As shown in Table 8, **AP** for different 20 classes of the PASCAL VOC 07&12 are reported. SBDet demonstrates a balanced and consistently high performance across various categories. Even in categories where SBDet does not achieve the highest AP, it is still competitive compared to models of comparable size.

Table 8: PASCAL VOC 07&12 test results. The highest **APs** for each class are indicated in **bold**.

Method	AP of 20 classes																				
	mAP	Aero	Bike	Bird	Boat	Bottle	Bus	Car	Cat	Chair	Cow	Table	Dog	Horse	Mbike	Person	Plant	Sheep	Sofa	Train	TV
Faster-RCNN	76.4	79.8	80.7	76.2	68.3	55.9	85.1	85.3	89.8	56.7	87.8	69.4	88.3	88.9	80.9	78.4	41.7	78.6	79.8	85.3	72.0
R-FCN	80.5	79.9	87.2	81.5	72.0	69.8	86.8	88.5	89.8	67.0	88.1	74.5	89.8	90.6	79.9	81.2	53.7	81.8	81.5	85.9	79.9
SSD300	77.5	79.5	83.9	76.0	69.6	50.5	87.0	85.7	88.1	60.3	81.5	77.0	86.1	87.5	83.9	79.4	52.3	77.9	79.5	87.6	76.8
SSD512	79.5	84.8	85.1	81.5	73.0	57.8	87.8	88.3	87.4	63.5	85.4	73.2	86.2	86.7	83.9	82.5	55.6	81.7	79.0	86.6	80.0
DSSD321	78.6	81.9	84.9	80.5	68.4	53.9	85.6	86.2	88.9	61.1	83.5	78.7	86.7	88.7	86.7	79.7	51.7	78.0	80.9	87.2	79.4
DSSD513	81.5	86.6	86.2	82.6	74.9	62.5	89.0	88.7	88.8	65.2	87.0	78.7	88.2	89.0	87.5	83.7	51.1	86.3	81.6	85.7	83.7
YOLOv8-n	78.6	86.5	88.0	75.1	69.9	65.3	85.3	90.6	85.3	61.0	81.0	75.3	81.1	89.2	86.0	87.0	50.9	77.2	73.4	88.2	76.2
YOLOv8-s	81.6	90.7	89.1	80.2	72.8	69.4	89.0	92.3	88.1	63.5	85.3	75.6	84.9	92.1	89.9	88.4	55.1	80.9	77.0	89.4	79.2
YOLOv8-m	83.7	92.2	92.7	83.2	74.7	73.6	89.1	92.7	91.2	67.4	87.0	78.5	87.3	92.7	90.4	89.2	59.5	80.6	80.7	89.9	81.7
YOLOv8-l	86.4	95.0	93.7	84.4	78.2	78.0	92.6	94.2	92.7	71.0	89.6	81.6	89.3	94.3	92.2	90.8	61.9	87.0	83.4	90.8	86.7
YOLOv8-x	86.9	93.5	93.9	86.1	79.1	77.5	92.6	94.3	92.2	72.3	89.8	83.2	90.9	94.7	92.5	90.8	64.5	87.7	84.3	91.7	86.3
SBDet-n	84.1	92.4	90.7	85.1	78.0	74.1	89.4	92.7	90.1	67.9	86.2	79.8	88.0	93.0	89.4	90.2	58.1	84.7	78.9	89.3	83.3
SBDet-s	86.0	94.0	93.0	85.6	79.1	76.3	91.0	94.0	92.8	69.8	89.1	80.6	90.6	93.1	91.7	91.7	64.1	86.6	79.8	91.7	84.3
SBDet-m	87.3	94.6	94.5	89.3	79.9	78.9	93.1	94.3	94.8	71.6	90.1	81.2	92.8	93.3	92.5	92.0	64.8	89.2	82.0	91.6	85.5

A.5 Analysis on YOLOv8-n-cl and R2Net-n on the Rotated MINIST (R.M.) dataset

This section compares the training accuracy of YOLOv8-n-cl and our R2Net-n on the R.M. dataset. We manipulate the training set by randomly rotating 60,000 images by 0, 90, 180, and 270 degrees while maintaining 10,000 images unaltered in the test set to evaluate the performance of a model under rotation. As depicted in Figure 9, both R2Net-n and YOLOv8-n-cl display fluctuations during training. However, R2Net-n exhibits milder fluctuations compared to the more pronounced oscillations observed in YOLOv8-n-cl. This contrast highlights the superior rotational anti-interference capability of R2Net-n, which is primarily attributed to its novel Relaxed Rotation-Equivariance (R.R.E.) property.

A.6 Visualization Analysis on Relaxed Rotation-Equivariance

In this subsection, we present a visualization of feature maps from our SBDet-n, as illustrated in Figure 10. We rotate the initial image (a) by 90, 180, and 270 degrees to generate images (b), (c), and (d) as inputs. It can be

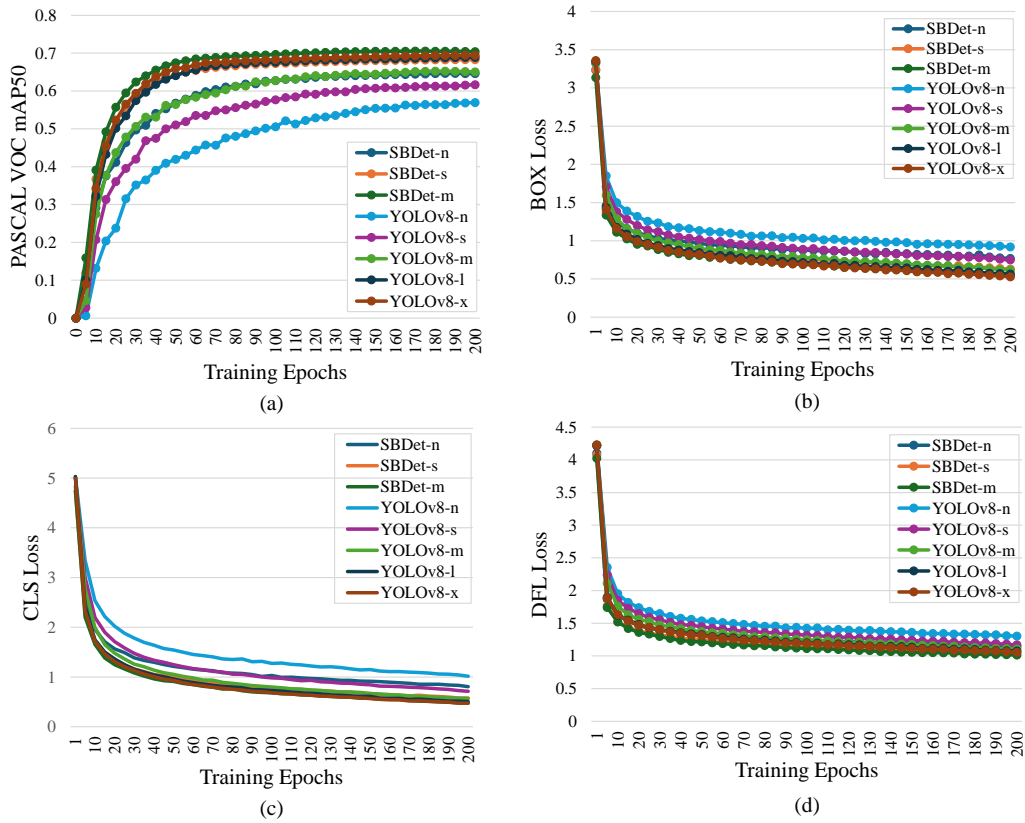


Figure 8: Comparison of YOLOv8 and our SBDet models. All models were trained on the PASCAL VOC dataset for 200 epochs with dual 4090 GPUs.

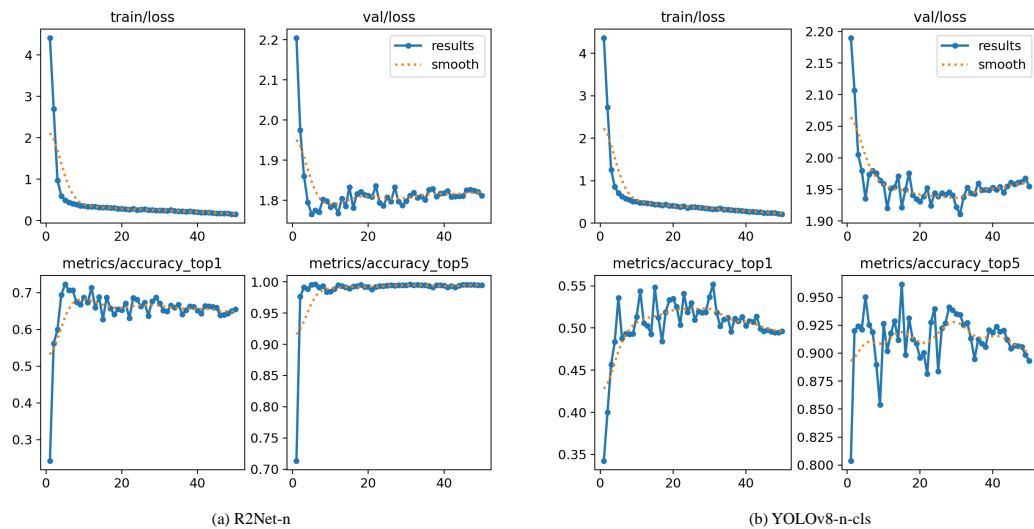


Figure 9: Comparison of YOLOv8-n and our R2Net-n in training accuracy on the R.M. dataset. Both models were trained for 50 epochs on dual 4090 GPUs with the resized input size 224×224 .

found that the output feature maps in (e), (f), (g), and (h), corresponding to each channel, exhibit consistency with minor variations, which demonstrates the Relaxed Rotation-Equivariance property of our network.

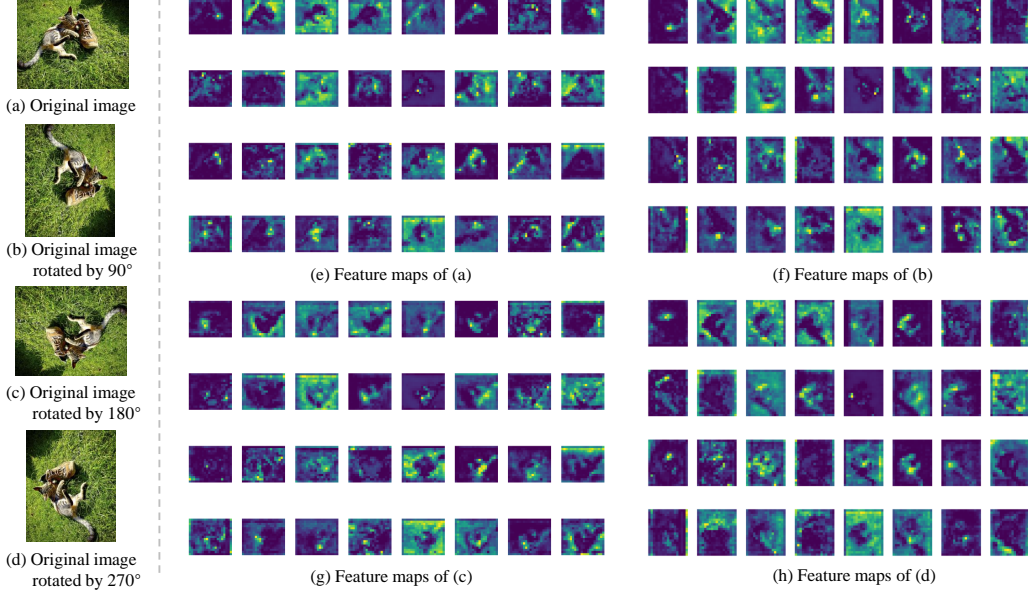


Figure 10: The SBDet-n feature map visualization of the original image rotated at (a) 0, (b) 90, (c) 180, and (d) 270 degrees, as depicted in (e), (f), (g), and (h), corresponds to its 32 channels.

A.7 Heatmap Visualization

In this section, we present the visualization of LayerCAM [24] heatmaps derived from YOLOv8-n, YOLOv7, YOLOv5, and our SBDet-n, as depicted in Figure 11. These heatmaps enable us to locate the regions of interest where the network concentrates its attention. It can be seen that YOLOv7 and our SBDet-n achieved better feature focusing. Notably, SBDet-n shows a comprehensive focusing range on certain objects, such as dogs and zebras. In contrast, YOLOv8 and YOLOv5 fail to exhibit such targeted feature focus on these particular objects.

A.8 Parameter Analysis of R2GConv and GConv based on the Rotation group C_4

Assuming the input channels, output channels, and kernel size of both R2GConv and GConv are c_{in} , c_{out} , and k , respectively. The parameters of our R2GConv can be calculated as follows:

$$c_{in} \times c_{out} \times 4 \times 1 \times 1 (\mathbf{R2PGConv}) + c_{out} \times 1 \times 1 \times k \times k (\mathbf{R2DGConv}) + 4 \times 2 \times 2 (\Delta) \approx 4 \times c_{in} \times c_{out} + k^2 \times c_{out} \quad (11)$$

where \cdot in (\cdot) denotes the source of parameters.

The parameters of GConv can be calculated as follows:

$$c_{in} \times c_{out} \times 4 \times k \times k = 4 \times c_{in} \times c_{out} \times k^2. \quad (12)$$

Therefore, the parameter of our R2GConv is only

$$\frac{4 \times c_{in} \times c_{out} + k^2 \times c_{out}}{4 \times c_{in} \times c_{out} \times k^2} = \frac{1}{k^2} + \frac{1}{4 \times c_{in}} \quad (13)$$

of GConv.

A.9 Limitation on Training Speed and Memory

Although SBDet has significant advantages in accuracy and parameter efficiency, the relatively slow training speed during R2GConv is primarily due to the involved group transformation operations, PointWise, and Depthwise operators, lacking optimization in CUDA. Additionally, the R2Net Block in the model, which incorporates residual concatenation, consumes a considerable amount of memory usage during training. Moving forward, specific CUDA operators can be developed to address the training speed issue and explore better construction methods for the R2Net Block.

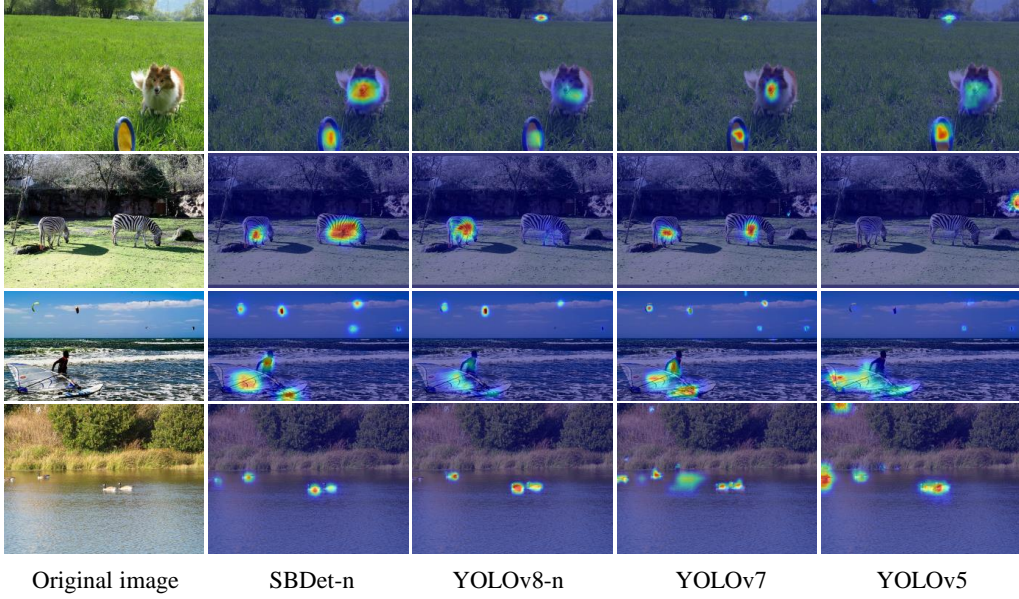


Figure 11: LayerCAM Heatmaps Visualizations: Neck Networks across YOLO Models (v8-n, v7, v5) and our Novel SBDet-n Architecture. Examples are from MS COCO Dataset

A.10 Theoretical Analysis

Since existing methods, including strictly rotation equivariant models, cannot perfectly tackle Symmetry-Breaking scenarios in object detection tasks, i.e., they can not learn an approximately equivariant function. We assume from [47] that the ground truth equivariant function Φ_{gt} is approximately equivariant. A model class with a similar degree of approximate equivariance would better approximate $\Phi_{relaxed}$ than Φ_{strict} a strictly equivariant class or a class without bias towards symmetry.

Firstly, the Equivariance Error (EE) quantifies how much the ground truth equivariant function Φ_{gt} is approximately equivariant. Let $\|\cdot\|$ denote the induced norm.

Definition A.1 (Equivariance Error [47]) Let $\Phi_{gt}: \mathcal{X} \rightarrow \mathcal{Y}$ be a function and G be a group. Assume that G acts on \mathcal{X} and \mathcal{Y} via representation $\rho^{\mathcal{X}}$ and $\rho^{\mathcal{Y}}$. Then the Equivariance Error of Φ_{gt} is

$$\|\Phi_{gt}\|_{EE} = \sup_{x,g} \|\rho^{\mathcal{Y}}(g)\Phi_{gt}(x) - \Phi_{gt}(\rho^{\mathcal{X}}(g)(x))\|.$$

Hence, Φ_{gt} is ϵ -approximately equivariant if and only if $\|\Phi_{gt}\|_{EE} < \epsilon$.

Proposition A.2 Let Φ_{gt} be ϵ -approximately equivariant and Lipschitz, with constant k . Then,

$$\|\rho^{\mathcal{Y}}(g) \cdot \Phi_{gt}(x) - \Phi_{gt}(x)\| \leq k\|\rho^{\mathcal{X}}(g) \cdot x - x\| + \epsilon, \forall g, x \in G \times \mathcal{X}.$$

Proof. If Φ_{gt} is Lipschitz with constant k , we have

$$\|\Phi_{gt}(\rho^{\mathcal{X}}(g) \cdot x) - \Phi_{gt}(x)\| \leq k\|\rho^{\mathcal{X}}(g) \cdot x - x\|, \forall g, x \in G \times \mathcal{X}.$$

From relaxed equivariance of g -, and triangle inequality, we find

$$\begin{aligned} \|\rho^{\mathcal{Y}}(g) \cdot \Phi_{gt}(x) - \Phi_{gt}(x)\| &\leq \|\rho^{\mathcal{Y}}(g) \cdot \Phi_{gt}(x) - \Phi_{gt}(\rho^{\mathcal{X}}(g)(x))\| \\ &\quad + \|\Phi_{gt}(\rho^{\mathcal{X}}(g)(x)) - \Phi_{gt}(x)\| \\ &\leq k\|\rho^{\mathcal{X}}(g) \cdot x - x\| + \epsilon, \forall g, x \in G \times \mathcal{X}. \end{aligned}$$

□

It is worth noting that both terms, $k\|\rho^{\mathcal{X}}(g) \cdot x - x\|$ and ϵ , collectively determine the overall upper limit of the equivariance error. The former term embodies the fundamental discrepancy inherently introduced by the

specific transformation actions, which naturally exist in the real world and are random. Hence, in this paper, we assume ρ as learnable permutations that can be modeled as variables following a normal distribution, i.e., $\Delta \sim \mathcal{N}(0, \sigma)$. These learnable transformations are also inherently norm-conserving, thereby allowing us to implicitly incorporate ρ into our considerations. Consequently, when an input x exhibits proximity to its transformed version, the outputs under a continuously equivariant function will also maintain close.

The following proposition further shows that the equivariance error of the $\Phi_{relaxed}$ will converge to the equivariance error of $\Phi_{gt} \|_{EE}$ as they converge in model error.

Proposition A.3 *Let $\Phi_{gt} : X \rightarrow Y$ be a function with $\|\Phi_{gt}\|_{EE} = \epsilon$. Assume $\|\Phi_{gt} - \Phi_{relaxed}\|_{\infty} \leq c$. Then $\|\|\Phi_{gt}\|_{EE} - \|\Phi_{relaxed}\|_{EE}\| \leq 2c + \epsilon$.*

Proof. By triangle inequality and invariance of the norm,

$$\begin{aligned} \|g \cdot \Phi_{relaxed}(x) - \Phi_{relaxed}(g \cdot x)\| &\leq \|g \cdot \Phi_{relaxed}(x) - g \cdot \Phi_{gt}(x)\| \\ &\quad + \|g \cdot \Phi_{gt}(x) - \Phi_{gt}(g \cdot x)\| + \|\Phi_{gt}(g \cdot x) - \Phi_{relaxed}(g \cdot x)\| \\ &\leq 2c + \epsilon. \end{aligned}$$

□